Advances in Geo-Energy Research

Vol. 19, No. 3, p. 268-284, 2026

Original article

Novel insights into the effect of drilling fluid particle size distribution on filter cake permeability

Mohammad S. Alosail, Razqan Razak, Khaliq I. Musa, Paula A. Gago, Zhixi Chen, Sheikh S. Rahman*

School of Minerals and Energy Resources Engineering, University of New South Wales, Sydney NSW 2052, Australia

Keywords:
Computational fluid dynamics
discrete element method
drilling fluid
filter cake
particle size distribution
permeability

Cited as:
Alosail, M. S., Razak, R., Musa, K. I., Gago, P. A., Chen, Z., Rahman, S. S. Novel insights into the effect of drilling fluid particle size distribution on filter cake permeability. Advances in Geo-Energy Research, 2026, 19(3): 268-284.
https://doi.org/10.46690/ager.2026.03.06

Abstract:
Understanding fluid-particle interactions is critical in petroleum engineering, particularly for controlling drilling fluid performance and mitigating fluid loss. Numerical methods, such as the coupled computational fluid dynamics discrete element method, enable a detailed investigation of these interactions without relying on extensive experimental testing. Traditional particle-sizing guidelines, including empirical bridging rules, provide only partial insights into the pore-scale mechanisms governing filter cake formation and permeability evolution. In contrast, numerical modelling directly resolves how the particle size distribution and solid concentration influence the filter cake structure and flow behavior. This study employed a coupled numerical simulation framework to examine filter cake formation for drilling fluids containing unimodal and bimodal particle size distributions across a range of solid concentrations. The key descriptors analyzed included the filtration rate, filter cake porosity, permeability, and pore size distribution. The results show that bimodal particle mixtures exhibit a concentration-dependent transition in permeability behavior. At lower solid loadings, bimodal systems maintain substantially higher permeability than unimodal systems because of the persistence of large, connected pore pathways formed by coarse particles. As the solid concentration increases, finer particles progressively infiltrate and occlude these pathways, leading to a marked permeability reduction and convergence toward unimodal behavior. Pore-size distribution analysis revealed that permeability is governed primarily by the connectivity and continuity of large pore throats rather than by bulk porosity. These findings demonstrate that bimodal distributions require sufficient fine content to achieve effective fluid loss control, providing pore-scale numerical guidance for optimizing drilling-fluid particle-size selection strategies.

1. Introduction

Oil and gas drilling accesses subsurface hydrocarbon reservoirs by creating boreholes (Aadnøy and Looyeh, 2019). Drilling fluid is used during this process to provide several important functions, one of which is to create a thin, low-permeability filter cake to prevent fluid loss to the formation. In highly permeable formations, this problem is often referred to as the loss of circulation. It can be defined as a significant and persistent loss of whole or partial fluid to the formation (Mitchell et al., 2011). In extreme cases, losses can cause depletion of the drilling fluid, which creates a potential hazard and may lead to well abandonment to avoid well blowout incidents (Skogdalen and Vinnem, 2012; Caenn et al., 2017). Drilling fluid solids include weighting agents that adjust the fluid density (Bland et al., 2006; Hossain, 2015) and active clays and polymers that control the rheology and filter cake properties (Bourgoyne et al., 1991; Caenn and Chillingar, 1996; Growcock and Harvey, 2005; Gautam and Guria, 2020). Controlling the particle-size distribution and

---

*Corresponding author.

E-mail address: m.alosail@student.unsw.edu.au (M. S. Alosail); m.abd_razak@student.unsw.edu.au (R. Razak); i.pg_musa@student.unsw.edu.au (K. I. Musa); paulaalejandrayo@gmail.com (P. A. Gago); zhixic@unsw.edu.au (Z. Chen).

Yandy Scientific Press

Received November 19, 2025; revised December 21, 2025; accepted January 13, 2026; available online January 16, 2026.

concentration is essential for forming low-permeability filter cakes without compromising the structural integrity in drilling and formation-sealing applications.

Early particle-sizing guidelines fundamentally oversimplified the bridging problem by relying on single-size criteria that ignored the complexity of filter cake formation. Abrams (1977) proposed that bridging agents should have a median diameter at least one-third of the median pore-size, with total solids concentration greater than or equal to 5 volume percent. The D90 criterion (Hands et al., 1998; Izyurov et al., 2019) suggests that the particle diameter below which 90 percent of particles fall should match the largest pore size, while the 2/3 rule (Yan and Feng, 2006) recommends particle sizes equal to approximately 2/3 of the pore diameter for optimal bridging. Although these simple correlations enable rapid design estimates for the minimum particle size, they fail to specify optimal size distributions and prove unreliable in formations with heterogeneous or variable permeability (Yan and Feng, 2006). The fundamental limitation of these early approaches was their inability to account for the interaction of particle populations to fill internal void spaces within the developing filter cake.

Recognizing that single-size particles cannot adequately seal complex pore structures, researchers have introduced multimodal particle strategies that combine distinct size populations to achieve more effective plugging. Luo and Luo (1992) developed the shielding temporary bridging technique, which employs rigid bridging particles with median diameters between 1/2 and 2/3 of the formation pore-size, supplemented by packing materials with median diameters approximately 1/4 of the pore-size at minimum concentrations of 30 kilograms per cubic meter and 15 kilograms per cubic meter, respectively. This combination minimizes filtrate invasion and reduces the penetration depth. Razavi et al. (2016) similarly demonstrated that bimodal distributions created by mixing coarse and fine graphite grades produced blends that were more effective than either unimodal grade alone. These methods represent important conceptual progress by acknowledging the need to balance coarse and fine particles; however, they remain largely empirical and cannot quantitatively resolve how particle interactions govern packing efficiency and permeability evolution.

Building upon the recognition that entire particle distributions, rather than isolated size fractions, control sealing performance, several comprehensive approaches have attempted to match complete size distributions to formation characteristics. The ideal packing theory (Dick et al., 2000) achieves a straight-line cumulative particle size distribution when plotted against the square root of the particle diameter by blending multiple particle sizes to seal the voids between the bridging particles. It typically uses 2-3 volume percent solids in unweighted fluids and 3-5 volume percent in weighted fluids. A key advantage of the ideal packing theory over the Abrams rule is its ability to define the particles required to seal the internal pore spaces created during bridging. Vickers et al. (2006) proposed matching the characteristic particle diameters describing the particle-size and pore-size distributions, whereas subsequent studies (Whitfill, 2008; Kumar et al., 2010) suggested selecting bridging materials whose median size corresponds to the predicted fracture width. While these distribution-based methods represent systematic advances in particle selection, they continue to depend on formation pore size estimates that are difficult to obtain and prove inadequate for formations with heterogeneous permeability structures.

The development of physics-informed analytical models has advanced the theoretical understanding by incorporating invasion dynamics and fractal geometry into particle-sizing frameworks. Suri and Sharma (2004) introduced a multicomponent filtration model that accounts for the simultaneous invasion of bridging particles, drilling solids, and polymers. Their results showed that coarse particles formed an initial skeletal framework, whereas smaller particles passed through and progressively reduced the permeability. The model predicts the return permeability and damage depth and recommends the selection of bridging materials that prevent the deep invasion of fine particles. You et al. (2018) proposed a fractal-based particle-sizing model, which showed that optimal sealing occurs when the fractal dimension of the particle-size distribution matches that of the formation pore structure. Experimental comparisons demonstrated that the fractal-based approach produced lower filtrate loss and achieved low filter cake permeability within 10 min. However, despite their theoretical sophistication, these models cannot explicitly simulate particle-level deposition processes, bridging mechanics, or the evolution of pore connectivity, which ultimately determine the filter cake microstructure and permeability.

Despite their contributions, all existing particle size distribution selection methods share a fundamental limitation: They are either empirical correlations or analytical models that cannot resolve the pore-scale mechanisms governing particle deposition, bridging, and filter-cake permeability. Empirical rules provide design estimates but lack mechanistic insight into how size distributions influence packing efficiency, void distribution and permeability evolution. Analytical models improve theoretical rigor but cannot capture the discrete particle-fluid interactions, contact forces, and geometric rearrangements that determine the cake microstructure. This gap motivates the use of pore-scale numerical approaches that can explicitly track particle motion and quantify emergent properties.

Coupled computational fluid dynamics and discrete element method modeling offer a numerical framework for capturing particle-fluid interactions at a high resolution (Golshan et al., 2020; Wang et al., 2023). The unresolved approach employed in this study computes the interphase forces through volume-averaged correlations, enabling the efficient simulation of thousands of particles while explicitly tracking the deposition and packing behavior (Wang et al., 2023). Razak et al. (2025) recently applied a spatially resolved variant of this coupled numerical framework to quantify filter cake growth and permeability in sand-screen retention systems. Their model was experimentally validated using micro-computed tomography imaging and laboratory permeability tests, demonstrating accurate predictions of pore structure and flow behavior. The present work extends this numerical framework to investigate filter cake development under varying particle size distributions and solid concentrations, using an unresolved approach to systematically evaluate porosity, permeability, and distribution-dependent mechanisms.

The application of coupled computational fluid dynamics and discrete element method simulations to filtration and pore plugging has revealed that filter cake properties emerge from complex interactions among particle characteristics, flow conditions, and pore geometry; however, prior studies have examined these factors largely in isolation rather than systematically. Investigations of particle-level variables demonstrate that size, morphology (Bérard et al., 2020; Duan et al., 2024), and sphericity (Deshpande et al., 2020) exert a strong influence on the void fraction and pressure drop across deposited layers, with decreasing particle sphericity initially increasing the pressure drop but ultimately decreasing it due to higher void fractions in filter cakes formed by nonspherical particles. Studies on nanoparticle plugging in shale pores further demonstrate that particle size and solid concentration strongly influence the plugging efficiency in fine pore networks (Yang et al., 2019). Flow condition studies have shown that the Reynolds number affects both the formation rate and sealing efficiency, where faster filter-cake formation at high Reynolds numbers paradoxically results in lower sealing efficiency and reduced fluid loss (Poletto et al., 2020). The initial fluid loss ratio critically determines particle penetration, with ratios of 5 percent preventing particle entry into porous regions, whereas ratios of 10 percent or higher allow effective plugging. Pore-scale geometry investigations reveal that tortuosity influences the velocity and flow volume of the liquid phase, which in turn affects particle entry into pore channels (Duan et al., 2024), whereas aperture dimensions impose critical thresholds that control particle capture behavior and determine whether particles experience long transport distances or rapid retention. Lin et al. (2022) showed that the clogging process evolves from isolated local blockages in specific regions to interconnected pore networks, emphasizing that the particle size distribution becomes particularly critical at the initial deposition stages. Pore morphology significantly affects retention mechanisms and wedging behavior, with complex pore structures providing an increased surface area that improves particle retention (Liu et al., 2023, Liu et al., 2024). Related simulations of fracture sealing also show that the sealing performance depends on the particle mechanical response and operating conditions, which influence the particle transport and retention behavior (Lee and Dahi Taleghani, 2020). These findings collectively establish that filter-cake development is governed by coupled particle-pore-flow interactions; however, no prior study has systematically integrated the size distribution structure with solid concentration to predict emergent filter-cake properties.

This represents a critical knowledge gap in the literature. Existing laboratory-based particle-size distribution guidelines, such as those proposed by Abrams, the shielding temporary bridging technique, and ideal packing theory (Abrams, 1977; Dick et al., 2000; Yan and Feng, 2006), identify the particle sizes required for initial bridging but cannot resolve pore-scale deposition dynamics, fine migration, or the evolution of connected pore pathways within the cake. No prior study using the coupled numerical approach has systematically evaluated how unimodal versus bimodal size distributions, combined with varying solid concentrations, jointly influence filter cake porosity, permeability, and pore-throat distributions under filtration conditions relevant to drilling operations. Experimental optimization is also limited by challenges in controlling particle-pore interactions and reproducing microstructural evolution at the pore scale.

To address these gaps, the present study employs a computational fluid dynamics and discrete element method numerical framework to systematically evaluate the effect of unimodal and bimodal particle-size distributions under varying solid concentrations on filter-cake formation on screen surfaces mimicking pore formation. By quantifying the porosity, permeability, pore throat distribution, and transient deposition mechanisms, this study provides pore-scale insight into how the size distribution structure governs the filter cake sealing efficiency. These findings support the development of improved particle size selection strategies for drilling fluid design.

2. Methodology

2.1 Description of the problem

This study simulated filter cake formation by drilling fluid particles using a coupled computational fluid dynamics and discrete element method framework. However, a fully resolved approach is not suitable for this study because of its high computational demand associated with fine mesh refinement. This limitation restricts the use of large numbers of particles (e.g., hundreds of thousands), which is necessary to investigate wide particle size distributions and their influence on filter cake formation. Therefore, an unresolved approach was adopted in this study.

Beyond computational feasibility, the unresolved approach is well-suited for this study for several methodological reasons. This enables the simulation of wide particle size distributions and large particle counts while maintaining particle-to-cell size ratios consistent with recommended practices. Previous applications of unresolved or volume-averaged formulations to filter cake formation and pore-clogging problems have shown that the method reliably predicts macroscopic quantities, such as porosity, permeability evolution, and cake growth trends, even though pore-scale flow details are not fully resolved.

However, the current approach introduces known modeling assumptions: The fluid field is cell-averaged, lubrication forces and near-particle shear are approximated, and particle-particle hydrodynamic interactions are not explicitly resolved. These simplifications influence the local microstructure but do not affect the objectives of this study, which focuses on the comparative permeability behavior between unimodal and bimodal particle-size distributions at the filter cake scale. Thus, the unresolved approach provides an appropriate balance between physical fidelity and computational feasibility for systematic particle size distribution evaluation.

Several adaptations were introduced to tailor the numerical setup for the filter cake simulations. One modification is the use of a flat filter instead of a plain square screen to overcome its limitations in retaining smaller particles (< 50 μm). Initially, the flat filter has no apparent thickness; however, as particles are deposited, a filter cake begins to form, allowing the permeability of the numerical filter cake to be estimated

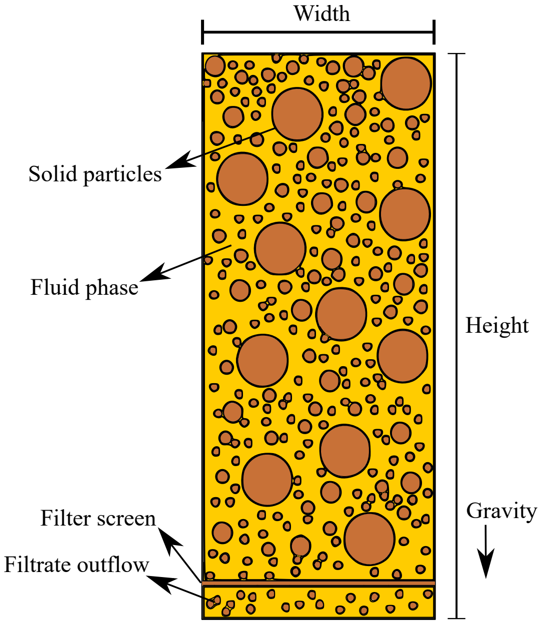

Fig. 1. Schematic representation of the simulation domain.

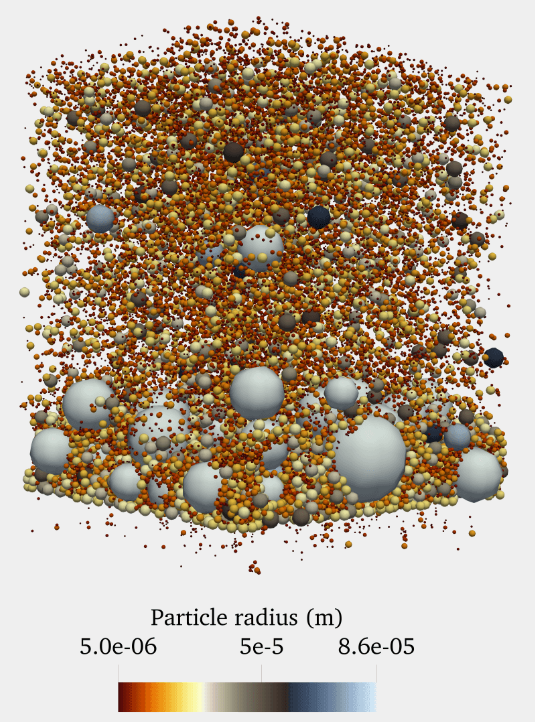

Fig. 2. Snapshot of the simulation domain.

independently of the screen.

The simulation domain was a 6 mm-high cube with a length and width of 4 mm. A flat filter was placed at the bottom to restrict the flow of particles falling under the influence of gravity. A schematic of the simulation domain is presented in Fig. 1. The filter cake buildup begins at the filter surface and grows upward as deposition progresses. Finer particles and filtrate pass through the filter during the early stages, with the flow becoming increasingly restricted as the cake develops. Solid particles were assumed to be spherical for a simplified representation of realistic drilling fluid particles. Fig. 2 shows a snapshot of the simulation domain, including the particle motion, cake deposition, and filtrate passing through the filter.

2.2 Overview of the numerical framework

The coupled framework used in this study to simulate the fluid-particle flow using an unresolved (volume-averaged) approach (Norouzi et al., 2016; Wang et al., 2023). In this framework, the computational fluid dynamics mesh resolution is larger than the individual particle sizes, with multiple particles occupying single computational cells. Fluid flow is computed by solving the volume-averaged Navier-Stokes equations using the finite volume method in OpenFOAM (Anderson and Jackson, 1967; Issa, 1986), whereas particle motion is computed by the discrete element method using LIGGGHTS (Cundall and Strack, 1979; Kloss and Goniva, 2011). The coupling accounts for fluid-particle interaction forces via drag models (Kuang et al., 2020), inter-particle contacts, and gravitational effects. Fig. 3 illustrates the fundamental differences between resolved and unresolved approaches (Kanitz and Grabe, 2019).

2.3 Numerical model description

The unresolved formulation adopted in this study follows Model A (Zhou et al., 2010; Norouzi et al., 2016), in which both the fluid and solid phases share the pressure field. Extensive studies have evaluated the applicability of different coupled framework formulations for various fluid-particle systems (Bouillard et al., 1989; Tsuji et al., 1993; Kafui et al., 2002; Di Renzo and Di Maio, 2007). Model A has been widely applied and validated for dense particulate flow and complex systems. The governing equations for particle motion and fluid flow are described below.

2.3.1 Movement of solid phase

The motion of the solid particles was represented by a discrete phase based on the soft-sphere model (Mindlin, 1949; Cundall and Strack, 1979). For an individual particle i, the translational and rotational equations of motion are as follows:

$$m_i \frac{\mathrm{d}v_i}{\mathrm{d}t} = f_i^{f-p} + \sum_{j\in CL_i} \left(f_{ij}^c + f_{ij}^{nc}\right) + f_i^g \tag{1}$$

$$I_i \frac{\mathrm{d}\omega_i}{\mathrm{d}t} = \sum_{j\in CL_i} M_{ij}^c + M_i^{f-p} \tag{2}$$

where m_i is the particle mass, v_i is the translational velocity, I_i is the moment of inertia, ω_i is the angular velocity, f_i^{f-p} is the fluid-particle interaction force, f_{ij}^c is the contact force from particle j or wall, f_{ij}^{nc} represents any additional non-contact interaction force included in the discrete element method formulation, $f_i^g = m_i g$ is the gravitational force, M_{ij}^c is the torque due to contact, and M_i^{f-p} is the torque arising from fluid-particle interactions, and t is time.

In the unresolved approach, the fluid-particle interaction force f_i^{f-p} is calculated using volume-averaged correlations that account for the drag and other hydrodynamic effects between the fluid and particle phases (Norouzi et al., 2016; Kuang et al., 2020).

Table 1. Comparative features of fully resolved and unresolved approaches.

Feature	Fully resolved (Direct/Explicit solution)	Unresolved (Volume-averaged)
Fluid flow model	The full Navier-Stokes equations are solved. The particles were part of the mesh.	Solves the averaged equations. The particles are represented by volume fraction.
How fluid responds to particles	The fluid velocity is adjusted inside each cell to match the particle velocity.	The fluid receives a force to slow down based on the relative velocity and particle concentration.
How particles receive fluid force	The net force originates from pressure and viscous stresses on the particle surface.	The net force is estimated from drag equations such as Wen-Yu (Niven, 2002) or Gidaspow (Gidaspow, 2004).
What links fluid and particle	The momentum exchange comes from the actual surface stress.	Momentum exchange is applied through drag equations.
Need for drag law	No drag law is required. Drag emerges from physics.	A drag law is required and must be selected by the user.
Particle shape and interaction	The particles have a complete geometry, and fluid flows around them.	The particles were treated as points. The surface effects were not resolved.
Trade-off	It has a higher accuracy but is slower to run.	It is faster to run with lower accuracy. This depends on the drag law quality.

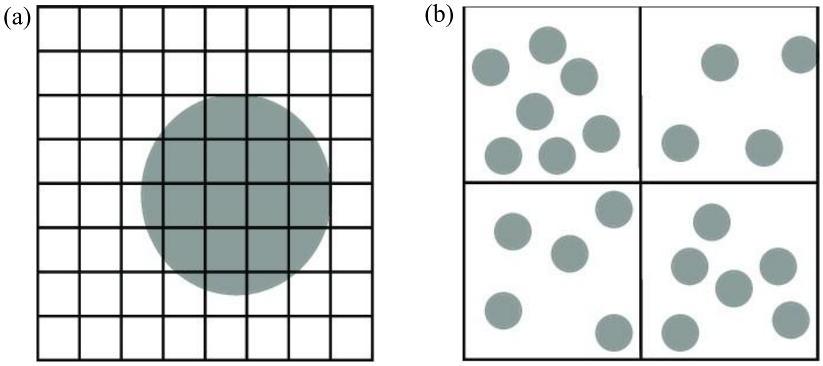

Fig. 3. Schematic representation of resolved and unresolved approaches. (a) Resolved approach, where particles are larger than grid cells. Accurately tracks each moving particle in the fluid domain. Mesh refinement is crucial. Grid size should be smaller than the smallest particle diameter. (b) Unresolved approach, where particles are smaller than grid cells. Tracks a group of moving particles in a grid within the fluid domain. Grid size must be large enough to include a sufficient number of particles to give a representative average.

2.3.2 Movement of fluid phase

The fluid-phase momentum conservation equation is derived from the volume-averaged formulation of Anderson and Jackson (1967):

$$\frac{\partial(\rho_f \varepsilon_f u)}{\partial t} + \nabla \cdot (\rho_f \varepsilon_f u u) = -\varepsilon_f \nabla p - \varepsilon_f \nabla \cdot \tau_f - F_A + \rho_f \varepsilon_f g \tag{3}$$

where ρ_f is the fluid density, ε_f is the fluid volume fraction, u is the fluid velocity, p is the pressure, τ_f is the viscous stress tensor of the fluid phase, g is the gravitational acceleration, and F_A is the volume-averaged fluid-particle interaction force.

The coupling force F_A is computed as follows:

$$F_A = \frac{1}{V_{cell}} \sum_{i=1}^{k_p} f_i^{f-p} \tag{4}$$

where V_{cell} is the computational cell volume, k_p is the number of particles within the cell, and f_i^{f-p} represents the fluid-particle interaction force acting on particle i, calculated using volume-averaged correlations.

The fluid phase continuity equation is as follows:

$$\frac{\partial(\rho_f \varepsilon_f)}{\partial t} + \nabla \cdot (\rho_f \varepsilon_f u) = 0 \tag{5}$$

Further details on unresolved formulations are provided in (Kloss et al., 2012; Norouzi et al., 2016; Duan et al., 2024). The fundamental differences between the resolved and unresolved approaches are summarized in Table 1 (Zhou et al., 2010; Sun and Xiao, 2016; Bérard et al., 2020; Ranjbari et al., 2025).

2.4 Parameter set-up of coupled framework

This study examined filter cake formation using six drilling fluid compositions with different particle size distributions and volume concentrations to evaluate the deposited filter cake permeability and filtrate loss. All samples consisted of spherical particles ranging from 10 to 630 μm. Fig. 4 shows

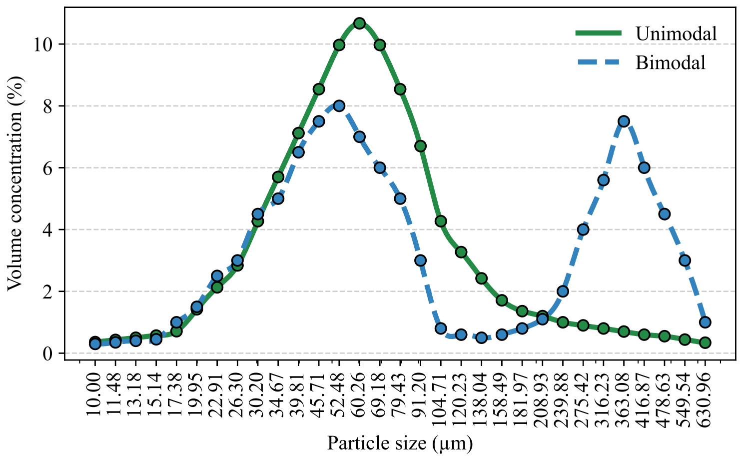

Fig. 4. Unimodal and bimodal particle size distribution.

the unimodal and bimodal particle size distributions used in this study. The first and second samples were composed of 2.5% particle volume concentration with unimodal and bimodal distributions, respectively. The third, fourth, fifth, and sixth samples were composed of 5% and 7.5% particle volume concentrations with bimodal and unimodal distributions, respectively. The numerical input parameters used in this study are listed in Table 2.

In the simulation domain, the number of particles was determined based on their particle size and volume concentration. Particles were randomly arranged within the domain from a point height of 0.25 to 6 mm, which is above the filter until the top point of the simulation domain. In the previously described simulation domain (Fig. 1), a constant pressure was applied at the inlet. This pressure value corresponds to the hydrostatic gauge pressure differential for this specific fluid and particle mixture. The outlet pressure was maintained at atmospheric gauge pressure to ensure a consistent hydrostatic pressure gradient throughout the domain. A slip boundary condition was implemented on the domain walls of the y- and z-planes. This enables the wall velocity to be proportional to the neighboring grid velocities tangential to the walls and helps reduce the finite size effect associated with small systems. Gravitational force, particle-fluid interactions, and grain-grain as well as grain-wall interactions influence particle movement. The soft-sphere model was used to calculate the intergranular forces (Ranjbari et al., 2025). The bottom of the simulation domain, located below the flat filter, was open, allowing the filtrate particles that passed through the filter cake and filter screen to exit the system.

The range of particle sizes used in the simulations was derived from the literature, based on the work of Caenn et al. (2017) on categorizing solid particles in drilling fluids. He explained that the solid particle sizes ranged from below 2 up to 2,000 μm and above. Owing to numerical limitations, a particle size range of 10 to 630 μm was chosen as a representative sample for average solid particles in drilling fluids. The filter was designed as a numerical barrier to stop the flow of particles larger than a previously determined threshold. For the purpose of this project, which is to examine the filter cake, the threshold was set at 50 μm, which is towards the lower end of the particle sizes chosen for this simulation. This allows particles smaller than 50 μm to pass through the barrier, while particles of size 50 or larger stop forming the first layer of the filter cake, while other particles plug and bridge over it.

3. Model benchmarking

The unresolved approach used in this study to simulate drilling fluid particle deposition on a filter was benchmarked against the resolved approach of Razak et al. (2025). In contrast to the original approach, which utilized a plain square screen, the present study used a flat filter. Benchmarking was performed by comparing the results of the resolved and unresolved approaches in the following sequence to assess the consistency in filter cake formation under different modeling resolutions and filter geometries:

1) Benchmarking of flat filter against plain square screen using spatially resolved approach.
2) Benchmarking of unresolved against spatially resolved approach using: The plain square screen, and the flat filter.

3.1 Benchmarking of flat filter against plain square screen

In this case, the deposition of the filter cake was simulated using a domain with dimensions and parameters identical to those reported by Razak et al. (2025) (Table 2). The objective was to compare the results between the plain square screen and flat filter configurations.

The volumetric flow rates of the fluid and particles for both filters are presented in Fig. 5. The flow rate initially peaked as the slurry reached the filter/screen, marking the onset of filter cake formation. Once the filter cake was established, the flow rate stabilized, reflecting a constant filtration rate. The peak filtration rate for the plain square screen was 4.18×10^{-6} m^3/s, which was slightly lower than the flat filter value of 4.81×10^{-6} m^3/s (Table 3). This difference was attributed to

Table 2. Numerical input parameters.

Reference	Parameters	Value
This study	Particle density (kg/m^3)	1,660
	Particle diameter (µm)	10-630
	Volume concentration of particles (%)	2.5; 5; 7.5
	Number of particles (bimodal)	94,634; 189,269; 283,903
	Number of particles (unimodal)	102,229; 204,458; 306,688
	Young's modulus (Pa)	10^8
	Poisson's ratio (-)	0.3
	Restitution coefficient (-)	0.15
	Friction coefficient (-)	0.5
	Particle solver time-step (s)	10^{-8}
	Fluid density (kg/m^3)	1,000
	Kinematic viscosity at 22 °C (m^2/s)	9.6×10^{-7}
	Fluid solver time-step (s)	10^{-6}
Razak et al. (2025)	Filter/screen pore size (µm)	180
	Particle density (kg/m^3)	1,660
	Particle diameter (µm)	120-630
	Particle size distribution type (-)	Unimodal
	Volume concentration of particles (%)	2
	Fluid density (kg/m^3)	1,000
	Viscosity (cp)	0.995

Table 3. Rate of filtration values for benchmarking.

Numerical approach	Filter type	Peak (10^{-6} m^3/s)	Steady state (10^{-6} m^3/s)
Resolved	Plain square	4.18	0.52
Unresolved	Plain square	6.42	2.75
Resolved	Flat	4.81	0.25
Unresolved	Flat	8.19	3.28

the wire thickness of the plain square screen, which impeded the fluid flow prior to cake formation. At steady state ($t = 1$ s), the flow rate decreased to 0.52×10^{-6} m^3/s for the plain square screen and 0.25×10^{-6} m^3/s for the flat filter.

The porosity profile of the filter cake was obtained by calculating the void fraction between the deposited particles (Fig. 6). The region between 0 and 0.28 mm reflects the influence of the filter geometry, whereas beyond this point, the porosity becomes relatively uniform, representing the bulk of the filter cake. The average bulk porosities of the plain square screen and flat filter were 41.53% and 41.14%, respectively, indicating close agreement between the two configurations. This similarity confirms that both filters yield comparable bulk cake structures despite differences in geometry.

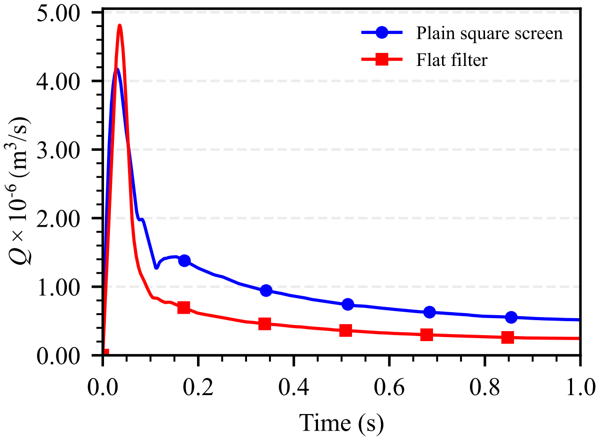

Fig. 5. Rate of filtration in the resolved approach for a pore size of 180 µm.

The permeability of the filter cake was measured using single-phase flow simulations in OpenFOAM's interFoam solver, following the methodology described in previous work by authors (Razak et al., 2025). Both cases maintained a consistent bulk region thickness of 5.0×10^{-4} m for an accurate permeability evaluation (Table 4). The permeability values were calculated as 82.88 D for the plain square screen and 65.08 D for the flat filter, which were consistent with their respective porosity values.

Table 4. Single-phase permeability for benchmarking purposes.

Numerical approach	Filter type	Filter cake bulk region (thickness) (10^{-4} m)	Pressure Difference (Pa)	Flow rate (10^{-7} m^3/s)	Permeability (D)
Resolved	Plain square	5.0	17.54	2.87	82.88
Unresolved	Plain square	5.0	15.57	2.80	91.07
Resolved	Flat	5.0	22.43	2.88	65.08
Unresolved	Flat	5.0	18.29	2.68	74.26

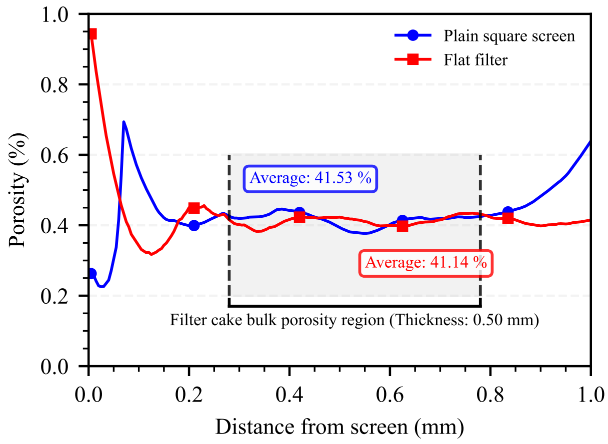

Fig. 6. Filter cake porosity profiles of a pore size of 180 μm.

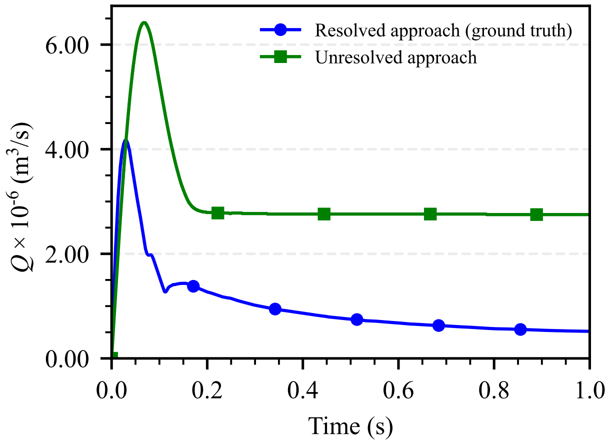

Fig. 7. Rate of filtration passing through the plain square screen (180 μm).

3.2 Benchmarking of unresolved and resolved approaches using a plain square screen

To benchmark the unresolved and resolved approaches, simulations were performed with a plain square screen using the same parameters as those listed in Table 2. The filtration rates are presented in Fig. 7. The resolved model captures detailed particle-fluid interactions by explicitly tracking each particle in a fluid mesh refined to approximately one-third of the mean particle diameter (Fig. 3). In contrast, the unresolved representation accounts for particle-fluid interactions by averaging across multiple particles within a grid cell, where each cell may contain 4-10 particles or more (Wang et al., 2023).

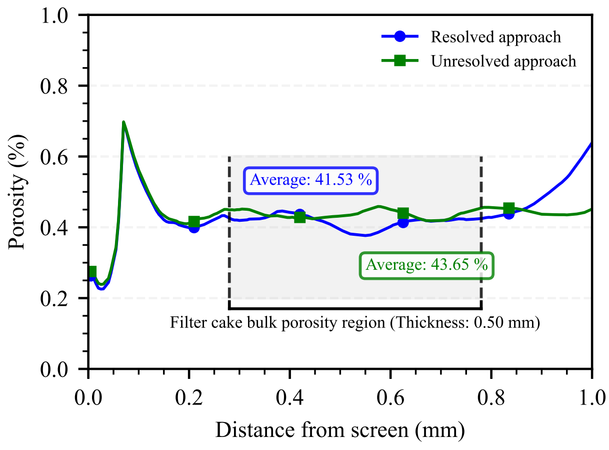

Fig. 8. Filter cake porosity profiles developed on the plain square screen (180 μm).

The unresolved solution recorded a higher initial peak flow rate of 6.42×10^{-6} m^3/s, compared to 4.18×10^{-6} m^3/s in the resolved model (an overestimation of 2.24×10^{-6} m^3/s; Table 3). By 0.2 s, the rates dropped to 2.79×10^{-6} m^3/s and 1.27×10^{-6} m^3/s, respectively. At steady state ($t = 1$ s), the unresolved model stabilized at 2.75×10^{-6} m^3/s, whereas the resolved model slowed to 0.52×10^{-6} m^3/s.

The porosity distributions of the filter cakes are presented in Fig. 8. Because both approaches use the same plain square screen geometry, the near-screen region (0-0.28 mm) exhibits a similar trend in porosity. Beyond this region, the porosity reaches a stable bulk value, providing a reliable basis for benchmarking. The resolved model yielded an average bulk porosity of 41.53%, whereas the unresolved model predicted 43.65%. This close agreement demonstrates that, despite the simplifying assumptions, the unresolved framework can reasonably reproduce the bulk structure of the filter cake. The slightly higher porosity in the unresolved case was consistent with its marginally higher permeability.

Permeability measurements (Table 4) show values of 82.88 D for the resolved solution and 91.07 D for the unresolved solution, corresponding to pressure differentials of 17.54 and 15.57 Pa.

3.3 Benchmarking of unresolved and resolved approaches using a flat filter

In this case, the unresolved approach was benchmarked against the resolved approach using a flat filter with the para-

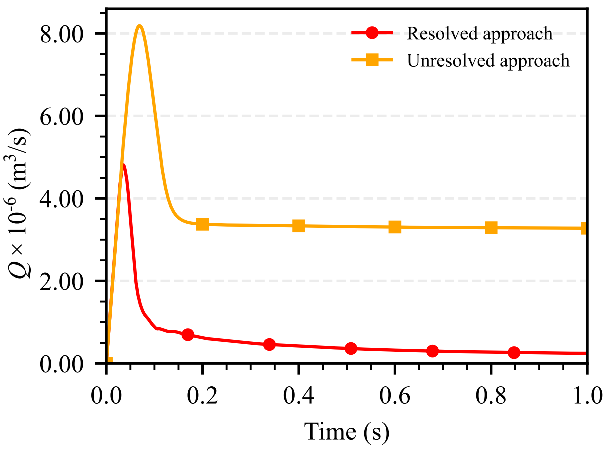

Fig. 9. Rate of filtration of particles and fluid passing through the flat filter (180 μm).

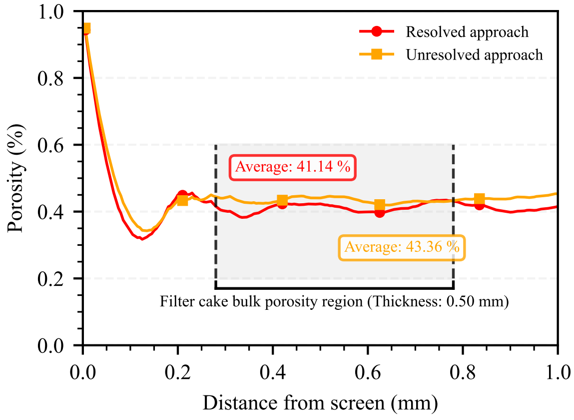

Fig. 10. Filter cake porosity profiles developed on the flat filter (180 μm).

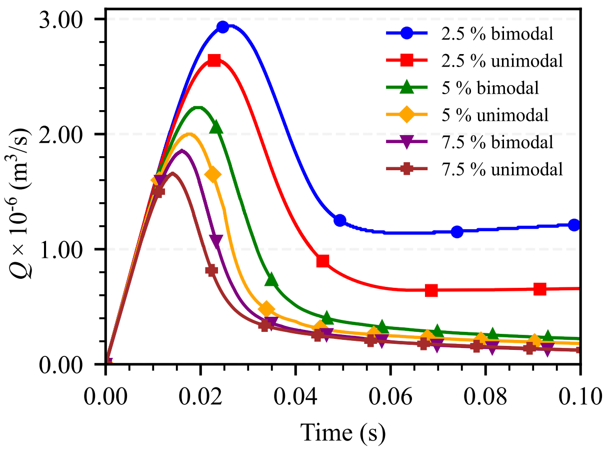

Fig. 11. Rate of filtration of particles and fluid passing through a 50 μm flat filter for unimodal and bimodal particle size distributions at 2.5, 5.0 and 7.5 vol.%.

Table 5. Peak filtration rate values.

Volume concentration (%)	Distribution type	Peak filtration rate value (10^{-6} m^3/s)
2.5	Unimodal	2.64 at 0.0221s
	Bimodal	2.94 at 0.0248s
5	Unimodal	2.00 at 0.0170s
	Bimodal	2.23 at 0.0186s
7.5	Unimodal	1.66 at 0.0139s
	Bimodal	1.86 at 0.0160s

meters listed in Table 2. The filtration rates are shown in Fig. 9. The unresolved exhibited a peak rate of 8.19×10^{-6} m^3/s, compared to 4.81×10^{-6} m^3/s for the resolved (Table 3). By 0.2 s, these values decreased to 3.37×10^{-6} m^3/s and 0.61×10^{-6} m^3/s, respectively. At steady state ($t = 1$ s), the unresolved simulation stabilized at 3.28×10^{-6} m^3/s, whereas the resolved case dropped to 0.25×10^{-6} m^3/s.

The porosity profiles are shown in Fig. 10. Unlike the plain square screen, the flat filter does not impose a strong geometric effect on the filter surface. Instead, particle deposition transitions smoothly into the bulk region, which is the most reliable basis for benchmarking the model. The resolved simulation yielded an average bulk porosity of 41.14% compared to 43.36% for the unresolved case. The $\sim 2.2\%$ difference indicates that the unresolved model slightly overestimates the pore space, although it still reproduces the bulk structure with reasonable accuracy. Permeability measurements (Table 4) confirmed this trend, with the unresolved simulation producing 74.26 D compared to 65.08 D in the resolved case, corresponding to pressure differentials of 18.29 and 22.43 Pa.

4. Results and discussion

This section presents the results of the numerical experiments in Table 2 using unimodal and bimodal particle size distributions (Fig. 4). Volume concentrations of 2.5%, 5%, and 7.5% were considered for particle sizes ranging from 10 to 630 μm. This study analyzed four descriptors of the filter cake: Filtration rate, porosity, permeability, and pore size distribution.

4.1 Rate of filtration

The filtration rates for all scenarios are shown in Fig. 11, and the corresponding peak values are listed in Table 5. Simulations were performed until steady-state conditions were reached. For the bimodal particle-size distributions, peak filtration occurred slightly later than in the unimodal cases. For example, at 2.5 vol.% particle concentration, the unimodal mixture reached its peak filtration rate of 2.64×10^{-6} m^3/s at 0.0221 s, whereas the bimodal case peaked at 2.94×10^{-6} m^3/s at 0.0248 s. This delay and higher peak magnitude can be explained by the presence of a greater fraction of coarse particles (≥ 275 μm) in bimodal mixtures. The delayed peak in the bimodal mixtures at low concentrations arises from the distinct settling dynamics of coarse and fine particle classes. Coarse particles, which have higher terminal settling velocities, settle more rapidly and reach the filter first, forming a loose initial framework with relatively large pore throats. This early stage structure permits a higher fluid throughput and contributes to a larger peak magnitude. Fine particles, which

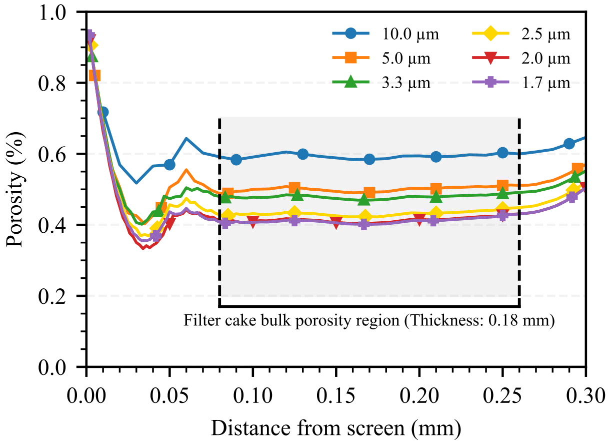

Fig. 12. Porosity sensitivity to grid-block size for the 5% unimodal case. The shaded band shows the bulk-porosity window (0.08-0.26 mm).

Table 6. Porosity sensitivity (bulk-region average, 0.08-0.26 mm).

Grid-block refinement (μm)/ grid block	Average bulk porosity	Difference in average porosities, Δε (from top to bottom)
10.0	0.5930	/
5.0	0.5000	0.0930
3.3	0.4790	0.0210
2.5	0.4320	0.0470
2.0	0.4140	0.0180
1.7	0.4110	0.0030

have significantly lower settling velocities, arrive later and progressively infiltrate the coarse framework, filling interstitial voids and narrowing throat pathways. The delayed arrival of the fine fraction postpones throat occlusion, causing the peak filtration rate to occur later in the bimodal system than in the unimodal case, where particles of similar size settle more uniformly and pack more quickly. This sequential settling mechanism explains both the elevated magnitude and delayed timing of the peak, as shown in Fig. 11 and Table 5. A similar trend was evident for 5 and 7.5 vol.% concentrations, although the higher solids loading shifts the peaks earlier and reduces their magnitude. An increase in the particle volume concentration also influences the timing and magnitude of the peak filtration rate. Higher concentrations led to earlier peak occurrence but lower peak values because of the larger mass of solids present at a constant fluid density. For example, in the unimodal mixtures, the peak filtration rate decreased from 2.64×10^{-6} m^3/s at 0.0221 s for 2.5 vol.% concentration to 1.66×10^{-6} m^3/s at 0.0139 s for 7.5 vol.% concentration. The 2.5 vol.% concentration cases are presented here for completeness but are not discussed further in subsequent sections, as the particle concentration was insufficient to generate a stable and thick filter cake.

Table 7. The average porosity of the bulk filter cake.

Volume concentration (%)	Distribution type	Filter cake bulk region (thickness, 10^{-4} m)	Average absolute bulk porosity (%)
5	Unimodal	1.8	43.18
	Bimodal	1.8	40.20
7.5	Unimodal	2.5	43.53
	Bimodal	2.5	38.91

4.2 Filter cake porosity

4.2.1 Grid resolution sensitivity analysis

Method. The filter cake porosity was computed from the particle coordinates by binarizing the bulk region into grid blocks and evaluating the void fraction. To assess the sensitivity to grid resolution, the analysis was repeated at $\Delta = 10$, 5, 3.3, 2.5, 2.0, and 1.7 μm per grid block for a representative case (5% unimodal), as shown in Fig. 12 and Table 6.

Observations. Near the screen (0-0.025 mm), all the curves overlap owing to the strong screen effect. Differences appear in the bulk region (0.08-0.26 mm) and diminish again as the cake approaches the upper boundary. Finer grids resolve particle packing and pore space more accurately, yielding a lower bulk porosity. The change from 10 to 5 μm was large, whereas the improvements became progressively smaller below 2.5 μm.

Resolution choice. Below $\Delta = 2.5$ μm, further refinement produces only minor reductions in bulk porosity while substantially increasing the cost. Therefore, $\Delta = 2.5$ μm per grid block was adopted for all porosity and permeability analyses.

4.2.2 Porosity profiles

The porosity profiles are shown in Fig. 13. In the near-screen region (~0-0.08 mm), the unimodal and bimodal curves overlapped, indicating similar early packing during initial settling. Beyond ~0.08 mm, within the bulk cake (0.08-0.26 mm at 5 vol.% and 0.08-0.33 mm at 7.5 vol.%), bimodal mixtures exhibit lower average porosity than unimodal (Table 7). At 7.5 vol.%, the bulk averages are 0.389 (bimodal) vs 0.435 (unimodal) ($\Delta = 0.046$). At 5 vol.%, they are 0.402 (bimodal) vs 0.432 (unimodal) ($\Delta = 0.030$).

This is consistent with packing theory: In bimodal systems, fine particles gradually fill the voids between coarse grains, producing a denser bulk cake. The earlier/later peak flow behavior in Section 4.1 corresponds to a transient stage in which larger pathways remain open; the bulk porosity reported here reflects the stabilized cake after fines have been infilled.

The concentration was increased from 5 to 7.5 vol.% causes only modest changes in bulk porosity ($\Delta \approx 0.003$ for unimodal; $\Delta \approx 0.013$ for bimodal). This weak sensitivity is expected because the particle size distribution remains constant, and porosity is primarily determined by particle size distribution rather than total particle count. The small reductions observed likely resulted from increased particle-particle

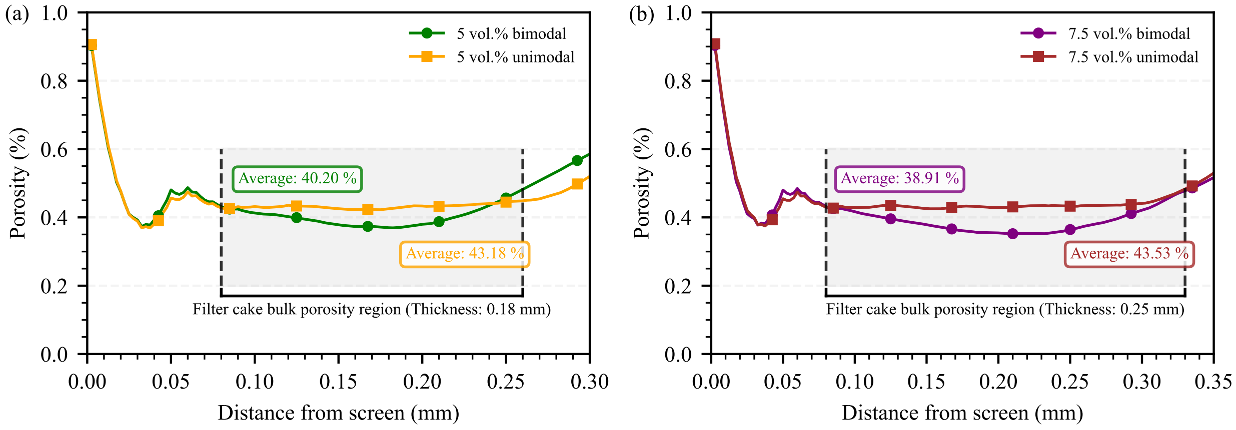

Fig. 13. Porosity profiles: (a) 5 vol.% and (b) 7.5 vol.% solids. The shaded bands denote the bulk-porosity window used for averaging.

Table 8. Single-phase flow permeability (Darcy) for unimodal and bimodal distributions at two volume concentrations. The permeability was evaluated using the same bulk window defined in Section 4.2.

Volume concentration (%)	Distribution type	Permeability (D)	Fraction of pores ≥ 40 μm (%)	Weighted fraction ≥ 40 μm (%)
5	Unimodal	1.07	7.5	16.1
	Bimodal	4.40	19.3	33.7
7.5	Unimodal	2.87	8.3	17.3
	Bimodal	2.96	13.5	26.5

interactions during settling, which provided more opportunities for particles to reach energetically favorable packing configurations. The slightly stronger response in bimodal distributions ($\Delta \approx 0.013$ vs. $\Delta \approx 0.003$) arises because fine particles can progressively migrate downward to fill coarse-mode voids as more material accumulates, a process that is less pronounced in unimodal distributions with narrower size ranges.

Note on interpretation: The porosity values represent the total void fraction in the bulk cake region (including both connected and isolated pores). Because permeability depends only on connected pore throats and their size distribution, bulk porosity and permeability are not directly correlated.

4.3 Filter cake permeability

The single-phase permeability was evaluated within the same bulk filter cake regions defined in Section 4.2, using a grid resolution of 2.5 μm to resolve the smallest pore throats. A representative example of the permeability evaluation domain is shown in Fig. 15 for 7.5 vol.% unimodal case, where particles within the bulk region are rendered opaque and particles outside this region are shown semi-transparent to indicate exclusion from the permeability calculation.

Two clear trends emerged from the permeability results summarized in Table 8. First, at 5 vol.% solids concentration, the bimodal mixture exhibits a substantially higher permeability than the unimodal mixture (4.40 vs. 1.07 D). Second, as the concentration increased from 5 vol.% to 7.5 vol.%, permeability increases markedly for the unimodal mixtures (from 1.07 to 2.87 D) but decreases for the bimodal mixtures (from 4.40 to 2.96 D), leading to convergence of permeability values at the higher concentration.

Although the bimodal mixtures exhibit lower bulk-averaged porosity than the unimodal mixtures at both concentrations (Section 4.2), this reduction in absolute porosity does not result in lower permeability. This apparent contradiction arises because permeability is governed primarily by the size, continuity, and connectivity of pore throats, rather than by the total void fraction alone. To clarify this relationship, Fig. 14 presents representative two-dimensional slices extracted from the mid-plane of the bulk filter cake region for all cases, with the slice-level porosity values indicated in each panel.

At 5 vol.%, the bimodal slice (Fig. 14(b)) exhibits visibly larger and more continuous pore openings compared with the unimodal slice (Fig. 14(a)), despite having lower local porosity (37.3% vs. 42.3%). These larger voids correspond to connected coarse-mode pore throats that remain insufficiently backfilled by fines at low concentrations, forming continuous percolating pathways across the cake. In contrast, the unimodal slice shows a greater abundance of small pores that increase the total porosity but contribute little to the through-flow owing to their limited connectivity and higher tortuosity. This structural distinction explains why the bimodal mixture at 5 vol.% maintains a permeability approximately four times higher than the unimodal case despite its lower bulk porosity.

The influence of concentration on permeability differs between unimodal and bimodal systems because of their

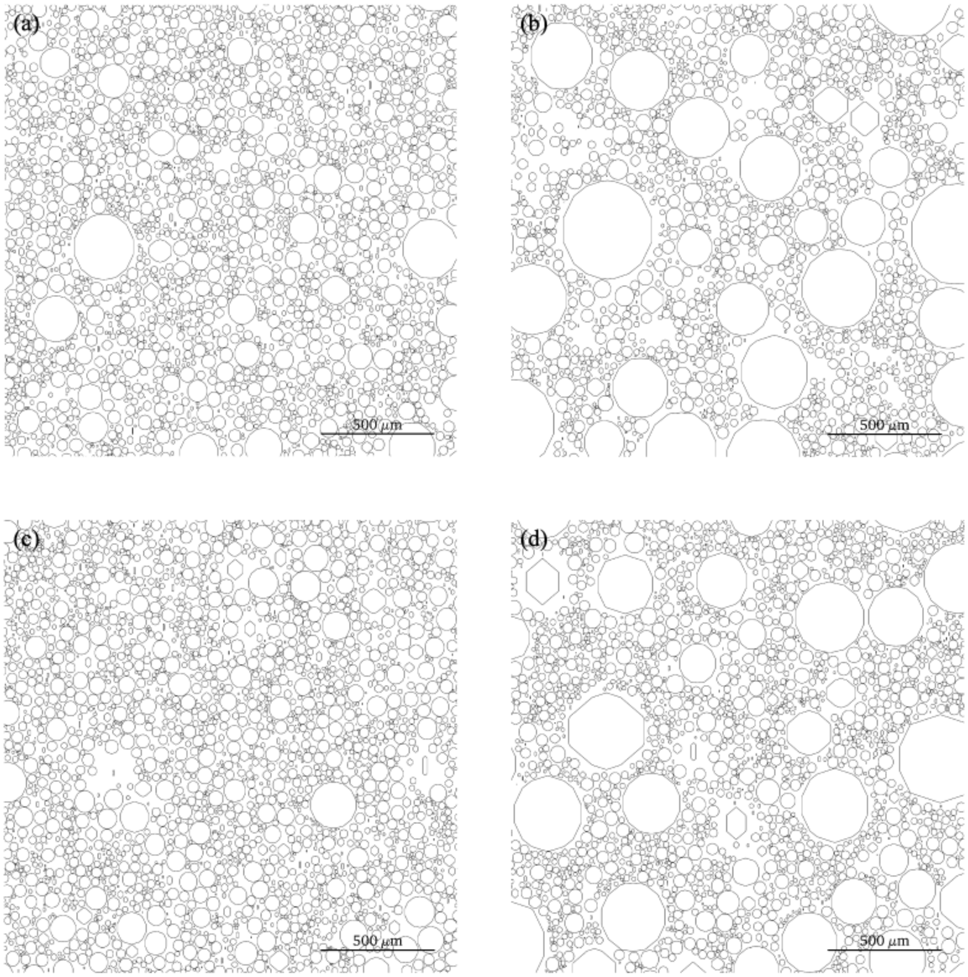

Fig. 14. Representative two-dimensional slices extracted from the mid-plane of the filter cake bulk region for the 5% and 7.5% volume concentrations with the following distributions: (a) 5% unimodal, (b) 5% bimodal, (c) 7.5% unimodal, and (d) 7.5% bimodal.

distinct packing and filling mechanisms. In unimodal mixtures, increasing the solids concentration from 5 to 7.5 vol.% leads to more rapid cake buildup and reduced opportunity for rearrangement and compaction. Consequently, connected vertical flow pathways persisted, increasing permeability, even though absolute porosity changed only marginally (from 43.18% to 43.53%). This behavior is consistent with the slice comparison in Figs. 14(a) and 14(c), which show similar local porosities but a visibly more open connected pore structure at higher concentrations.

In contrast, bimodal mixtures respond differently to increasing concentrations. At 7.5 vol.%, additional fine and medium particles progressively infiltrate and partially occlude the coarse-mode pore throats that dominate permeability at 5 vol.%. This is reflected in Fig. 14(d), where large pores remain present but are more frequently interrupted and less continuously connected than in the 5 vol.% bimodal slice (Fig. 14(b)). The reduction in the connectivity of these large throats leads to a decrease in permeability, despite only a modest reduction in bulk porosity.

This behavior is quantitatively captured by the large-pore statistics reported in Table 8. At 5 vol.%, the bimodal mixtures exhibit a 2.6-fold higher fraction of pores larger than 40 μm compared with the unimodal mixtures (19.3% vs. 7.5%), which corresponds to the fourfold difference in permeability. At 7.5 vol.%, the fraction of pores ≥40 μm decreases for the bimodal mixtures (from 19.3% to 13.5%) and increases slightly for the unimodal mixtures (from 7.5% to 8.3%), leading to convergence of permeability values near 3 D. These trends confirm that permeability is controlled by the connectivity and continuity of large pore throats rather than absolute porosity alone.

This interpretation is consistent with the discussion in Section 4.2, where permeability is shown to be governed by the connectivity and tortuosity of pore throats rather than by total porosity alone (Safari et al., 2016). Similar observations have been reported in pore-scale studies using the coupled framework of particle plugging in shale pores (Yang et al., 2019) and in numerical investigations of colloid retention in complex pore morphologies (Liu et al., 2023), where the flow is controlled by a limited subset of connected, high-conductivity pathways.

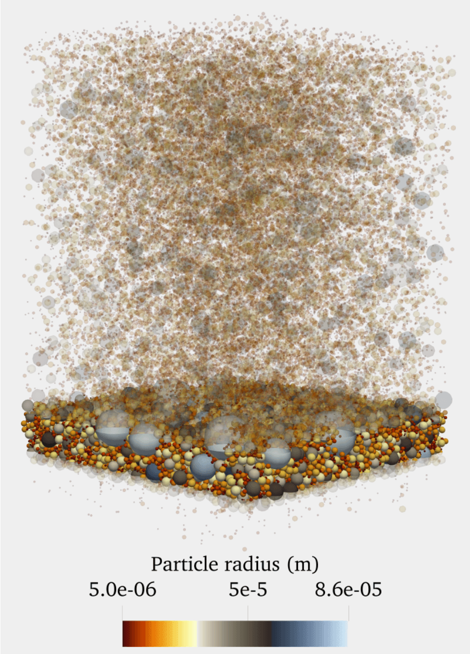

Fig. 15. Representative visualization of the filter cake bulk region used for permeability (7.5 vol.% unimodal).

Overall, the combined analysis of bulk porosity profiles (Section 4.2), slice-level porosity visualizations (Fig. 14), and particle size distributions (Section 4.4) demonstrates that the total porosity is a weak predictor of permeability in these systems. Instead, the permeability is governed by a subset of connected pore throats that form continuous flow pathways through the filter cake. The direct three-dimensional quantification of connected porosity and pore-network topology would further strengthen this interpretation and is identified as valuable future work.

4.4 Pore size distribution of filter cake

To reconcile the differences observed between porosity and permeability, the pore-size distribution was quantified by slicing the filter cake bulk region (as defined in Section 4.2), binarizing each slice at a fine spatial resolution, and extracting pore-size metrics representative of pore bodies and connecting throats. The pore size distributions for all cases are shown in Fig. 16. Across all cases, the pore-size distribution exhibited a dominant mode near 20 μm. At a given solids' concentration, the unimodal (particle size) mixtures displayed a higher proportion of small pores than the bimodal mixtures, whereas the bimodal mixtures showed minor secondary peaks and a larger tail above 40 μm, corresponding to hydraulically dominant pore throats. Quantitative analysis revealed that at 5 vol.%, 19.3% of bimodal pores exceed 40 μm compared to only 7.5% for unimodal, a 2.6-fold difference (Table 8).

Changes in the concentration affect the pore-size distribution differently for unimodal and bimodal mixtures. Unimodal cakes exhibited a pronounced increase in the fraction of pores ≥40 μm when the concentration was increased from 5 to 7.5 vol.% (from 7.5% to 8.3%), preserving larger flow channels. In contrast, bimodal cakes showed a reduction in the ≥40 μm fraction with a higher concentration (from 19.3% to 13.5%), consistent with fines and medium particles progressively filling the coarse-mode voids and tightening the throat network. These pore-size distribution shifts align with the permeability trends in Section 4.3: The 2.6-fold difference in large-pore fraction at 5 vol.% corresponds to the 4-fold permeability difference, while the convergence of large-pore fractions at 7.5 vol.% (8.3% vs 13.5%) matches the permeability convergence (∼2.9 D).

This analysis also clarifies why the absolute porosity was higher in the unimodal cases despite their lower permeability at 5 vol.%: Unimodal cakes contain more abundant small pores that raise the mean porosity but contribute little to through-flow, whereas the relative abundance and connectivity of larger pores in bimodal cakes govern permeability more directly. Because permeability depends on connected pore throats and their sizes (effective porosity and tortuosity), a one-to-one correlation with absolute porosity is not expected to be observed.

4.5 Comparison with empirical guidelines

These numerical findings provide mechanistic insights into the empirical particle-sizing rules developed from laboratory experiments. Abrams' bridging rule (Abrams, 1977) and the shielding temporary bridging technique (Yan and Feng, 2006) focus on matching particle the median particle diameter to pore throat sizes to initiate bridging, typically requiring 5% by volume or more of appropriately sized solids. The results support this concentration threshold; at 5 vol.%, unimodal mixtures achieved effective sealing (1.07 D), while bimodal distributions remained highly permeable (4.40 D) due to insufficient fines to occlude large pore throats. Only at 7.5 vol.% did both particle size distributions converge to comparable permeability (∼2.9 D), confirming that a minimum fines concentration is required for bimodal effectiveness.

Razavi et al. (2016) demonstrated that bimodal particle size distributions (2/3 coarse, 1/3 fine) achieve superior fracture sealing compared to unimodal distributions in lost circulation applications. The pore-scale simulations extend this understanding by revealing that the bimodal performance is concentration-dependent; the 2/3 coarse: 1/3 fine ratio may require total concentrations > 5 vol.% for filter cake applications, as the 5 vol.% bimodal case failed to control permeability despite having the recommended size distribution proportions. The quantified large-pore fractions (Table 8) directly demonstrate how an elevated large-pore fraction (19.3% of pores >40 μm in the bimodal case versus 7.5% in the unimodal case at 5 vol.%) leads to persistent high-permeability pathways.

Furthermore, while Suri and Sharma (2004) conceptually described how bridging particles initially allow smaller particles to pass through before fines reduce cake permeability, the numerical simulations directly visualized and quantified this process. The delayed peak in bimodal filtration (Section 4.1), pore-size distribution evolution (Section 4.4), and permeability trends (Section 4.3) capture the transition from coarse-particle bridging to fine-particle pore filling, providing the pore-scale physics underlying the macroscopic observations.

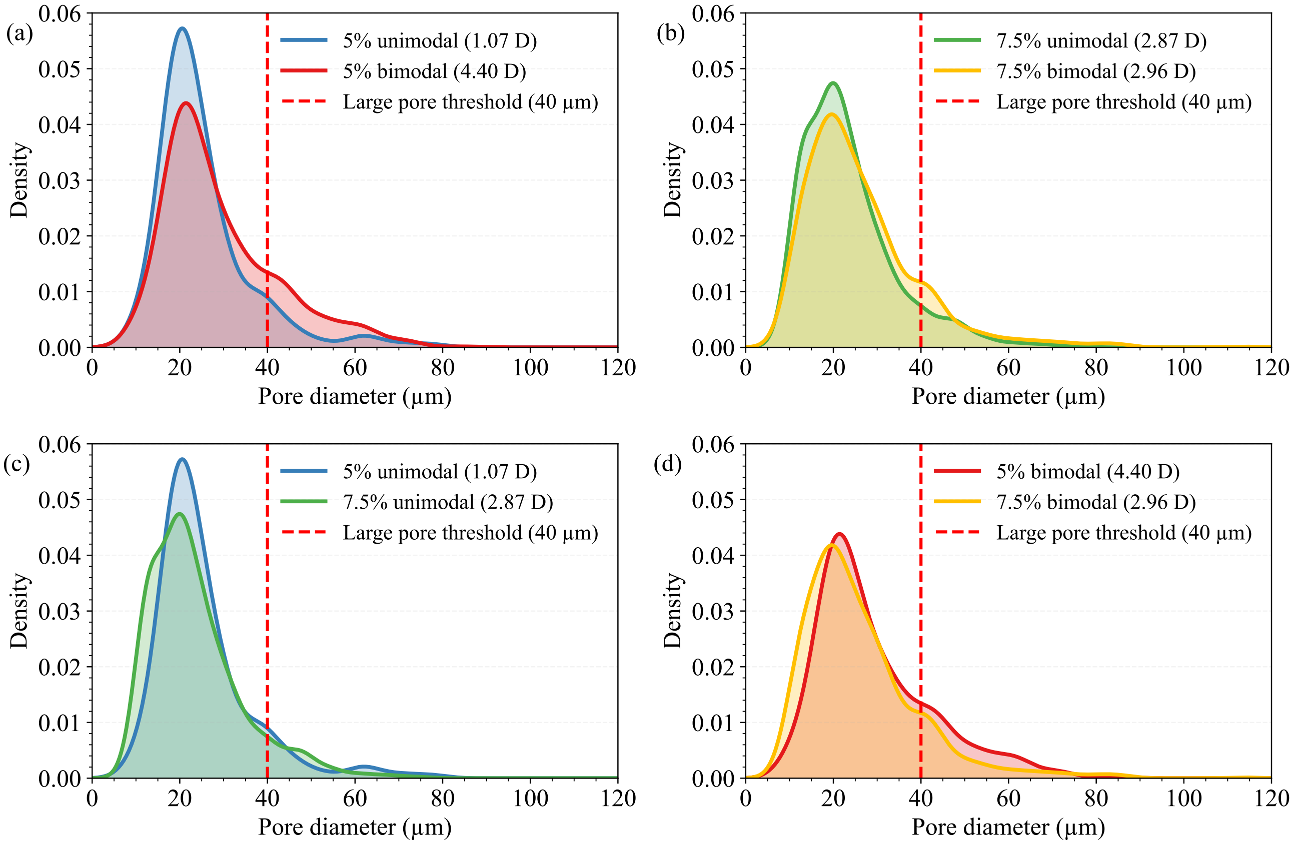

Fig. 16. Filter cake pore size distributions. Top row: Unimodal vs. bimodal at (a) 5 vol.% and (b) 7.5 vol.% solids. Bottom row: Concentration effect within (c) unimodal and (d) bimodal mixtures. The vertical dashed line marks the 40 μm threshold used to quantify the fraction of large pores discussed in this study.

These pore-scale results can also be directly translated into practical drilling-fluid formulations. The simulations show that bimodal blends require a minimum fine fraction to effectively occlude the coarse-mode pore throats that dominate the permeability at low concentrations. At 5 vol.%, the bimodal mixture contains insufficient fines to occlude the > 40 μm voids (19.3% large-pore fraction), resulting in persistent high-permeability pathways. The solid loading was increased to 7.5 vol.% supplies enough fines to reduce the large-pore fraction to 13.5% and achieve permeability similar to the unimodal case (~2.9 D). Thus, bimodal formulations are effective only when the fines fraction is sufficiently high to suppress coarse-mode connectivity. This finding aligns with empirical recommendations that fines should constitute at least ~30%-40% of the solid mass for reliable bridging and sealing in particulate lost circulation material systems. Therefore, the numerical results provide a pore-scale justification for these guidelines and offer quantitative thresholds for practical design.

4.6 Limitations and future work

4.6.1 Limitations

Mechanistic clarification related to particle shape and generalizability: The assumption of perfectly spherical particles primarily affects the quantitative magnitude of porosity and permeability but does not alter the governing pore-scale mechanisms identified in this study. Spherical particles tend to pack less densely and interlock less effectively than angular or irregular particles, which can lead to higher porosity and an overestimation of absolute permeability relative to real drilling-fluid solids. However, the key mechanisms observed here, formation of a coarse-particle framework, fines-driven occlusion of pore throats, and the resulting concentration-dependent permeability reversal, are controlled by pore-throat connectivity and continuity rather than particle shape alone. Because angular or irregular particles would be expected to further restrict throat connectivity through enhanced mechanical interlocking, these mechanisms are expected to remain qualitatively valid, and potentially more pronounced, for non-spherical particle systems.

The conclusions of this study should be interpreted in light of the following modeling assumptions:

1) Spherical, noncohesive particles were used. Real drilling solids often include angular, plate-like, or polymeric particles that interlock more strongly and may reduce permeability relative to predictions (Deshpande et al., 2020).
2) Particle size range limited to 10-630 μm, excluding colloids and ultra-fines (< 10 μm) that contribute to cake consolidation in field muds.
3) Unresolved numerical approach, where fluid fields are

volume-averaged and hydrodynamic interactions (lubrication, near-wall shear, particle-particle flow perturbations) are represented through empirical drag/lift laws rather than fully resolved flow.

4) The filter is represented as a uniform barrier retaining ≥ 50 μm particles, which mimics a fine screen rather than a heterogeneous reservoir rock pore system.

These factors may affect the absolute permeability values. However, the mechanistic trends identified, that is, coarse-framework formation, fines-driven throat occlusion, and concentration-dependent permeability reversal between unimodal and bimodal particle-size distributions, are governed by general pore-throat connectivity principles and are therefore expected to remain qualitatively robust.

4.6.2 Future work

Future extensions of this study may address the following:

1) Non-spherical particle geometries (angular, rod-like, and plate-like) were used to quantify the sensitivity of permeability and packing to morphology.
2) Cohesive or polymer-treated particles represent realistic mud additives and chemical interactions during cake consolidation.
3) Broader particle size ranges, including ultra-fines (< 10 μm), are required to capture the full role of colloids in late-stage sealing.
4) Direct quantification of connected porosity using 3D pore-network extraction can strengthen the interpretation of permeability results.
5) Filtration against heterogeneous formation-like pore structures, rather than a uniform screen, was explored for applicability to reservoir rock filtration regimes.

These developments will enhance the quantitative predictive capability while building on the mechanistic insights demonstrated in this study.

5. Conclusions

This study used numerical methods to investigate the effects of unimodal and bimodal distributions and solid concentration (2.5-7.5 vol.%) control filter-cake structure and permeability for particles between 10 and 630 μm retained on a 50 μm screen. The key findings are as follows:

1) The solid concentration determines whether an effective low-permeability cake can be formed. At 2.5 vol.% solids, both distributions produce open, highly permeable cakes. These cases were included for completeness but were not representative of effective fluid-loss control.
2) At 5 vol.% solids, unimodal and bimodal systems show fundamentally different filtration dynamics. Unimodal distributions rapidly form a dense cake with an early peak filtration velocity and a stabilized permeability of ≈ 1.07 D. Bimodal distributions form a coarse structural framework that delays cake consolidation and yields much higher permeability (≈ 4.40 D), driven by persistent large flow channels between coarse particles that fines cannot fully bridge at this concentration level.
3) At 7.5 vol.% solids, unimodal and bimodal cakes converge to similar low permeabilities. Increasing the solids concentration supplies sufficient fines for bimodal systems to occlude the large pore throats formed by coarse particles. Both distributions then stabilized near ≈ 2.9 D, despite retaining different internal microstructures.
4) Permeability depends on the connected pore throat structure, not the bulk porosity. The bulk porosity varied only slightly across concentrations, but the permeability changed dramatically. Bimodal cakes at 5 vol.% retain a larger fraction of connected throats larger than 40 μm, sustaining high flow despite similar total porosity to unimodal cakes. This distinction strengthens the conclusion that connected porosity governs the flow behavior.
5) Practical design guidelines for bimodal blends. Bimodal distributions are not inherently inferior; however, they require sufficient fines to seal the large throats created by coarse particles. In this study:
    - At 5 vol.% solids, the fines fraction ($\approx 20\%$-25% of solids) was insufficient, yielding high permeability.
    - Effective sealing occurred only when solids concentration exceeded 5 vol.%, or fines constituted $\sim 30\%$-40% of the solids by volume, enabling throat occlusion. Unimodal distributions achieved low permeability even at 5 vol.% because the narrow distribution suppresses large, connected voids.
6) Relation to empirical particle size rules. Unimodal results align with Abrams' rule and ideal packing theory; however, bimodal blends highlight an additional requirement absent from traditional guidelines: Fines fraction and solids concentration must be specified, not only single-value particle size descriptors (e.g., characteristic diameters) commonly used to describe particle size distributions.

Acknowledgements

This study did not receive any specific grants from funding agencies. The first author acknowledges the support of Saudi Aramco through the PhD scholarship. Computational resources were provided by the UNSW High-Performance Computing Facility, Katana (DOI: 10.26190/669X-A286).

Additional information: Author's email

sheik.rahman@unsw.edu.au (S. S. Rahman)

Conflicts of interest

The authors declare no competing interest.

References

Aadnøy, B. S., Looyeh, R. Petroleum Rock Mechanics: Drilling Operations and Well Design. Houston, USA, Gulf Professional Publishing, 2019.

Abrams, A. Mud design to minimize rock impairment due to particle invasion. Journal of Petroleum Technology, 1977, 29(5): 586-592.

Anderson, T. B., Jackson, R. Fluid mechanical description of fluidized beds. Industrial & Engineering Chemistry Fundamentals, 1967, 6(4): 527-539.

Bérard, A., Patience, G. S., Blais, B. Experimental methods in chemical engineering: Unresolved CFD-DEM. The Canadian Journal of Chemical Engineering, 2020, 98(2): 424-440.

Bland, R., Mullen, G., Gonzalez, Y., et al. HP/HT drilling fluids challenges. Paper SPE 103731 Presented at IADC/SPE Asia Pacific Drilling Technology Conference, Bangkok, Thailand, 13-15 November, 2006.

Bouillard, J. X., Lyczkowski, R. W., Gidaspow, D. Porosity distributions in fluidized beds with immersed obstacle. AIChE Journal, 1989, 35(6): 908-922.

Bourgoyne, A. T., Millheim, K. K., Chenevert, M. E., et al. Applied Drilling Engineering. Houston, USA, Society of Petroleum Engineers, 1991.

Caenn, R., Chillingar, G. V. Drilling fluids: State of the art. Journal of Petroleum Science and Engineering, 1996, 14(3): 221-230.

Caenn, R., Darley, H. C. H., Gray, G. R. Composition and Properties of Drilling and Completion Fluids. Oxford, UK, Gulf Professional Publishing, 2017.

Cundall, P. A., Strack, O. D. L. Discrete numerical model for granular assemblies. Géotechnique, 1979, 29(1): 47-65.

Deshpande, R., Antonyuk, S., Iliev, O. DEM-CFD study of the filter cake formation process due to nonspherical particles. Particuology, 2020, 53: 48-57.

Di Renzo, A., Di Maio, F. P. Hydrodynamic stability of fluidized beds in CFD-DEM. Chemical Engineering Science, 2007, 62(1-2): 116-130.

Dick, M. A., Heinz, T. J., Svoboda, C. F., et al. Optimizing selection of bridging particles for reservoir drilling fluids. Paper SPE 58793 Presented at SPE International Symposium on Formation Damage Control, Lafayette, Louisiana, USA, 23-24 February, 2000.

Duan, Y., Dong, X., Yang, H., et al. Solid-liquid drilling fluid flowing through fracture-vuggy medium: Pore-scale structure reconstruction and large-scale simulation. Geoenergy Science and Engineering, 2024, 236: 212761.

Gautam, S., Guria, C. Optimal synthesis and performance evaluation of high-pressure high-temperature polymer-based drilling fluid: The effect of viscoelasticity on cutting transport, filtration loss, and lubricity. SPE Journal, 2020, 25(3): 1333-1350.

Gidaspow, D. Multiphase Flow and Fluidization: Continuum and Kinetic Theory Descriptions. San Diego, USA, Academic Press, 2004.

Golshan, S., Sotudeh-Gharebagh, R., Zarghami, R., et al. Review and implementation of CFD-DEM applied to chemical process systems. Chemical Engineering Science, 2020, 221: 115646.

Growcock, F., Harvey, T. Drilling fluids, in Drilling Fluids Processing Handbook, edited by Growcock, F. and Harvey, T., Gulf Professional Publishing, Houston, pp. 15-68, 2005.

Hands, N., Kowbel, K., Maikranz, S., et al. Drill-in fluid reduces formation damage. Oil and Gas Journal, 1998, 96(28): 65-68.

Hossain, M. E. Fundamentals of Sustainable Drilling Engineering. Hoboken, USA, John Wiley & Sons, 2015.

Issa, R. I. Solution of implicitly discretised flow equations by operator-splitting. Journal of Computational Physics, 1986, 62(1): 40-65.

Izyurov, V., Valiullin, I., Shako, V., et al. Selecting bridging agents' PSD for optimum plugging while drilling. Paper D023S034R001 Presented at SPE Russian Petroleum Technology Conference, Moscow, Russia, 22-24 October, 2019.

Kafui, K. D., Thornton, C., Adams, M. J. Discrete particle-continuum modelling of gas-solid fluidised beds. Chemical Engineering Science, 2002, 57(13): 2395-2410.

Kanitz, M., Grabe, J. Influence of the installation process of piles on the soil in the vicinity from numerical simulation. Paper V001T10A019 Presented at ASME 2019 38th International Conference on Ocean, Offshore and Arctic Engineering, Glasgow, Scotland, UK, 9-14 June, 2019.

Kloss, C., Goniva, C. LIGGGHTS - Open source discrete element simulations of granular materials based on Lammps, in Supplemental Proceedings: Materials Fabrication, Properties, Characterization, and Modeling, edited by TMS, John Wiley & Sons, Hoboken, pp. 781-788, 2011.

Kloss, C., Goniva, C., Hager, A., et al. Models, algorithms and validation for opensource DEM and CFD-DEM. Progress in Computational Fluid Dynamics, An International Journal, 2012, 12(2-3): 140-152.

Kuang, S., Li, K., Yu, A. CFD-DEM modelling and simulation of pneumatic conveying: A review. Powder Technology, 2020, 365: 186-207.

Kumar, A., Savari, S., Whitfill, D. L., et al. Wellbore strengthening using LCM properties. Paper SPE 133484 Presented at SPE Annual Technical Conference and Exhibition, Florence, Italy, 19-22 September, 2010.

Lee, L., Dahi Taleghani, A. Fracture-Hole Systems: How Can Microholes Improve Fracture Complexity and Proppant Distribution? SPE Production & Operations, 2020, 35(4): 752-765.

Lin, Y., Fang, Y., He, C. Numerical investigation of the particles flow behavior in a proppant fracture using the CFD-DEM method. Tunnelling and Underground Space Technology, 2022, 128: 104622.

Liu, S., Shikhov, I., Cui, Y., et al. Pore-scale study of the influence of particle shape on colloid-facilitated contaminant transport using CFD-DEM. Geoenergy Science and Engineering, 2023, 227: 211772.

Liu, S., Shikhov, I., Arns, C. H. Mechanisms of colloid-facilitated contaminant transport in fractured porous media from high-resolution CFD-DEM simulations. Transport in Porous Media, 2024, 151(4): 831-851.

Luo, X., Luo, P. The application study of shielding temporary bridging technology in formation damage control. Drilling & Completion Fluids, 1992, 9(3): 19-27.

Mindlin, R. D. Compliance of elastic bodies in contact.

Journal of Applied Mechanics, 1949, 16: 259-268.

Mitchell, R. F., Miska, S., Aadnøy, B. S. Fundamentals of Drilling Engineering. Richardson, USA, Society of Petroleum Engineers, 2011.

Niven, R. K. Physical insight into the Ergun and Wen & Yu equations for fluid flow in packed and fluidised beds. Chemical Engineering Science, 2002, 57(3): 527-534.

Norouzi, H. R., Zarghami, R., Sotudeh-Gharebagh, R., et al. Coupled CFD-DEM Modeling: Formulation, Implementation and Application to Multiphase Flows. Hoboken, USA, John Wiley & Sons, 2016.

Poletto, V. G., De Lai, F. C., Junqueira, S. L. M. Computational fluid dynamics and discrete element method applied to solids holdup calculation in fluidized beds. Journal of the Brazilian Society of Mechanical Sciences and Engineering, 2020, 42: 376.

Ranjbari, P., Ebrahimi, M., Ein-Mozaffari, F., et al. A comprehensive review of packed bed radial flow reactors for the chlorination of Ti-bearing materials: CFD-DEM and experimental studies. Powder Technology, 2025, 454: 120677.

Razak, R., Alosail, M. S., Musa, K. I., et al. Spatially resolved CFD-DEM model for upscaling sand retention testing to field-scale inflow control devices. Powder Technology, 2025, 449: 120406.

Razavi, O., Karimi Vajargah, A., van Oort, E., et al. Optimum particle size distribution design for lost circulation control and wellbore strengthening. Journal of Natural Gas Science and Engineering, 2016, 35: 836-850.

Safari, A., Dowlatabad, M. M., Hassani, A., et al. Numerical simulation and X-ray imaging validation of wormhole propagation during acid core-flood experiments in a carbonate gas reservoir. Journal of Natural Gas Science and Engineering, 2016, 30: 539-547.

Skogdalen, J. E., Vinnem, J. E. Quantitative risk analysis of oil and gas drilling, using Deepwater Horizon as case study. Reliability Engineering & System Safety, 2012, 100: 58-66.

Sun, R., Xiao, H. SediFoam: A general-purpose, open-source CFD-DEM solver for particle-laden flow with emphasis on sediment transport. Computers & Geosciences, 2016, 89: 207-219.

Suri, A., Sharma, M. M. Strategies for sizing particles in drilling and completion fluids. SPE Journal, 2004, 9(3): 337-348.

Tsuji, Y., Kawaguchi, T., Tanaka, T. Discrete particle simulation of 2D fluidized bed. Powder Technology, 1993, 77(1): 79-87.

Vickers, S., Cowie, M., Jones, T., et al. A new methodology surpassing current bridging theories. Wiertnictwo Nafta Gaz, 2006, 23(1): 501-515.

Wang, X., Gong, L., Li, Y., et al. Developments and applications of the CFD-DEM method in particle-fluid numerical simulation in petroleum engineering: A review. Applied Thermal Engineering, 2023, 222: 119865.

Whitfill, D. Lost circulation material selection and fracture modeling. Paper SPE 115039 Presented at SPE International Symposium and Exhibition on Formation Damage Control, Scheveningen, The Netherlands, 27-29 May, 2008.

Yang, X., Chen, S., Shi, Y., et al. CFD-DEM modelling of particle plugging in shale pores. Energy, 2019, 174: 1026-1038.

Yan, J., Feng, W. Design of drill-in fluids by optimizing bridging particles. Paper SPE 104131 Presented at SPE International Symposium and Exhibition on Formation Damage Control, Lafayette, Louisiana, USA, 15-17 February, 2006.

You, L., Tan, Y., Kang, Y., et al. Optimizing the particle size distribution of drilling fluids based on fractal characteristics for applications in horizontal wells. Journal of Petroleum Science and Engineering, 2018, 171: 1223-1231.

Zhou, Z. Y., Kuang, S. B., Chu, K. W., et al. Discrete particle simulation of particle-fluid flow: Model formulations and their applicability. Journal of Fluid Mechanics, 2010, 661: 482-510.